REVIEW OF SCIENTIFIC INSTRUMENTS **84**, 125111 (2013)

Design, analysis and testing of a parallel-kinematic high-bandwidth XY nanopositioning stage

Chun-Xia Li, Guo-Ying Gu, Mei-Ju Yang, and Li-Min Zhu[a]
State Key Laboratory of Mechanical System and Vibration, School of Mechanical Engineering, Shanghai Jiao Tong University, Shanghai 200240, China

(Received 22 July 2013; accepted 30 November 2013; published online 23 December 2013)

This paper presents the design, analysis, and testing of a parallel-kinematic high-bandwidth XY nanopositioning stage driven by piezoelectric stack actuators. The stage is designed with two kinematic chains. In each kinematic chain, the end-effector of the stage is connected to the base by two symmetrically distributed flexure modules, respectively. Each flexure module comprises a fixed-fixed beam and a parallelogram flexure serving as two orthogonal prismatic joints. With the purpose to achieve high resonance frequencies of the stage, a novel center-thickened beam which has large stiffness is proposed to act as the fixed-fixed beam. The center-thickened beam also contributes to reducing cross-coupling and restricting parasitic motion. To decouple the motion in two axes totally, a symmetric configuration is adopted for the parallelogram flexures. Based on the analytical models established in static and dynamic analysis, the dimensions of the stage are optimized in order to maximize the first resonance frequency. Then finite element analysis is utilized to validate the design and a prototype of the stage is fabricated for performance tests. According to the results of static and dynamic tests, the resonance frequencies of the developed stage are over 13.6 kHz and the workspace is 11.2 μm × 11.6 μm with the cross-coupling between two axes less than 0.52%. It is clearly demonstrated that the developed stage has high resonance frequencies, a relatively large travel range, and nearly decoupled performance between two axes. For high-speed tracking performance tests, an inversion-based feedforward controller is implemented for the stage to compensate for the positioning errors caused by mechanical vibration. The experimental results show that good tracking performance at high speed is achieved, which validates the effectiveness of the developed stage. [http://dx.doi.org/10.1063/1.4848876]

I. INTRODUCTION

With the capabilities of nanometer positioning accuracy, nanopositioning stages are widely used in many industrial applications, such as scanning probe microscopy (SPM),[1–3] lithography,[4] nano-manipulation and manufacturing,[5,6] and biological science.[7,8] Flexure-based mechanisms, which have advantages of no friction, no backlash, compact and monolithic structure, and ease of fabrication, are usually employed in nanopositioning stages to provide smooth motions by their elastic deformation.[9] The piezoelectric actuators (PZTs) are widely adopted to drive flexure-based mechanisms due to their advantages of ultra-high resolution, fast response, and large stiffness.[10]

Recently, high-speed nanopositioning systems are increasingly required,[11,12] especially in the fields of high-throughput nano-manufacturing and biological molecules studying. However, the available operating speed of a nanopositioning system is limited by the resonance frequencies of the nanopositioning stage. Therefore, it is necessary to design stages with high resonance frequencies.

In the past few years, many high-bandwidth nanopositioning stages have been developed.[2,3,7,11,13–15] According to the kinematic structures, these stages can be classified into two categories: the serial-kinematic positioners (SKPs) and the parallel-kinematic positioners (PKPs). SKPs usually adopt a structure with one-degree-of-freedom nanopositioner nested in another one.[3,7,13] Such configuration allows for a relatively high resonance frequency in one axis which makes the SKPs more suitable for the raster scanning in SPMs. However, the SKPs generally have disadvantages of cumulative error and parasitic motion such as runout or guiding error.[13] Compared with SKPs, there is no cumulative error for PKPs and it is easy to measure and correct for the parasitic motion. Moreover, the PKPs have advantages of low inertia, high stiffness, and compactness. When appropriately designed, PKPs can be developed with low-coupling or nearly decoupling performance.[10,16] Therefore, the PKPs are more popular in nanopositioning stages with high resonance frequencies.[2,11,14]

To improve the mechanical resonance frequencies of the PKPs, the most common practice is to make the stage rigid and compact. However, when the stiffness of the flexure-based mechanism is increased for high resonance frequencies, two important issues come along. First, the stiffness and maximum displacement of the stage are contradictive. In other words, the increase in stiffness results in the reduction of the maximum travel range of the stage. For instance, a PKP is proposed with relatively high resonance frequencies over 8.8 kHz, but the travel range of this PKP is only 6.5 μm × 6.6 μm for X- and Y-axis.[14] There is a PKP with both high resonance frequency (22 kHz) and large travel range

---

[a] Electronic mail: zhulm@sjtu.edu.cn.

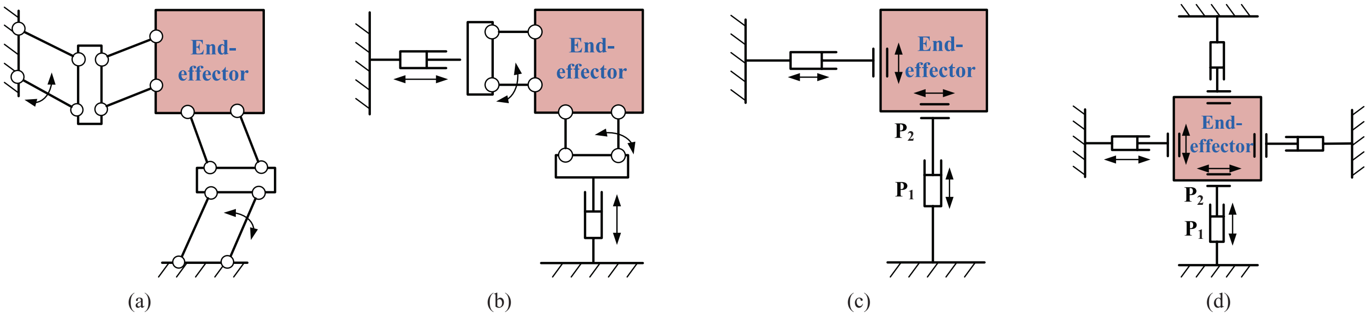

FIG. 1. The possible parallel mechanisms for XY stages.

(13 μm × 13 μm).[2] However, 8 PZTs are used in X- and Y-axis arranged in a push-pull configuration, which would cost high-power and high-bandwidth voltage amplifiers to drive these PZTs. Second, the stiffness and accuracy are contradictive performances of flexures.[11,17] Simply scaling up the dimensions of flexures for high stiffness would bring in undesired error motions (e.g., parasitic motion and cross-coupling) due to the load-stiffening and elastokinematic effects.[17] The low cross-coupling or decoupling PKPs usually have relatively low mechanical resonance frequencies. As has been reported, a PKP is developed with decoupled performance between X- and Y-axis and restricted parasitic rotations in XY plane, but the first resonance frequency of the PKP is relatively low (approximately 8 kHz).[11] Therefore, it is a challenging work to design a PKP with high resonance frequencies, large travel range, and low cross-coupling performance. In the past, few stages satisfying all these performance requirements are proposed.

In this paper, a parallel-kinematic piezo-actuated XY nanopositioning stage is developed for high-speed and high-precision positioning and tracking. The stage meets the demand for high resonance frequencies, relatively large travel range, and nearly decoupled performance between two axes. In the developed stage, there are two kinematic chains. In each kinematic chain, the end-effector is connected to the fixed base by two symmetrically distributed flexure modules, respectively. Each flexure module is composed of a fixed-fixed beam and a parallelogram flexure which are adopted as two orthogonal prismatic joints. Different from the commonly used constant rectangular cross-section beam,[2,11,14] a novel center-thickened beam is proposed in this paper to act as the fixed-fixed beam. The benefit for such a development lies in the fact that it has large stiffness which contributes to improving the resonance frequencies of the developed stage. The center-thickened beam also reduces the cross-coupling between two axes and restricts undesired parasitic motion. To decouple the motion in two axes totally, a symmetric configuration is employed for the parallelogram flexures. Besides the excellent performance, the developed stage has advantages of simple and compact structure and ease of manufacturing.

The remainder of the paper is organized as follows. In Sec. II, the details of the mechanical design are presented, and static and dynamic models of the developed stage are established. In Sec. III, the design considerations are discussed, and the dimensional optimization is performed. Then, the finite element analysis (FEA) of the mechanism with optimized dimensions is carried out to evaluate the performance of the developed stage. Sec. IV presents the experimental setup and static and dynamic performance tests. High-speed tracking tests are carried out with the inversion-based feedforward approach to confirm the effectiveness of the developed stage. After that, conclusions are drawn in Sec. V.

II. MECHANICAL DESIGN AND ANALYSIS OF THE STAGE

A. Mechanical design

For a parallel-kinematic XY nanopositioning stage, it has to ensure the independent translational motion along X- and Y-axis. Thus, the end-effector of the stage can achieve motion along any direction on the XY plane. Several possible two-degree-of-freedom translational parallel mechanisms[10,16,18,19] are shown in Fig. 1. For the mechanism (a),[18] each of its kinematic chains consists of two serially connected parallelogram joints. In the mechanism (b),[19] each kinematic chain is composed of a prismatic joint and a parallelogram joint. The parallelogram joints can keep the orientation of the end-effector invariant when the stage is actuated along one axis. However, undesired cross-coupling error along the other axis is generated at the same time, as depicted in Fig. 2(a), which makes it difficult for the kinematic analysis and control of such a stage. The mechanism (c)[10,16] adopts two orthogonal prismatic joints for each kinematic chain and it is totally decoupled as long as ideal prismatic joints are used. Compared with the mechanisms (a) and (b), mechanism (c) is a better kinematic scheme for the developed XY stage.

According to the structural concept above, the key point is to design ideal prismatic joints for P$_1$ and P$_2$ shown in Fig. 1(c). For prismatic joint P$_1$ connected to the fixed base directly, a fixed-fixed beam is a good choice and is widely used,[2,11,14] as it has much lower stiffness in the working direction than the other directions. However, it is difficult to find an ideal flexure joint for prismatic joint P$_2$ which is connected to the end-effector. The most commonly used flexure prismatic joints are shown in Fig. 2. Though the flexures shown in Figs. 2(a) and 2(b) actually belong to parallelogram joints, they are usually used as prismatic joints.[16] Compared with the parallelogram flexure on one side shown in Fig. 2(a), the double parallelogram flexures on one side shown in Fig. 2(b) reduce the cross-coupling by utilizing a serial connection of two parallelogram flexures, but there still exists small cross-coupling error. With a symmetric distribution of the flexures

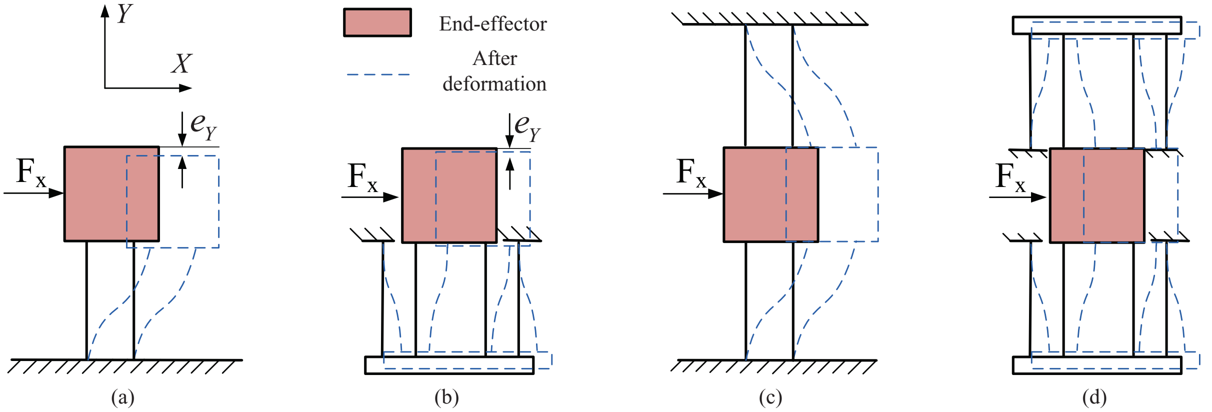

FIG. 2. Flexure prismatic joints. (a) Parallelogram flexure on one side. (b) Double parallelogram flexures on one side. (c) Parallelogram flexures on two sides. (d) Double parallelogram flexures on two sides.

about the actuating axis, flexures shown in Figs. 2(c) and 2(d) eliminate the coupling error completely, and thus the symmetric flexures could be regarded as two ideal prismatic joints. Compared with the parallelogram flexures on two sides shown in Fig. 2(c), the double parallelogram flexures on two sides shown in Fig. 2(d) have smaller stiffness which would result in lower mechanical resonance frequencies. As the stage is designed for high mechanical resonance frequencies, the parallelogram flexures on two sides depicted in Fig. 2(c) are chosen for P_2. Since the flexures are equal to two flexure prismatic joints, the kinematic structure of the XY stage in this paper is further improved as the mechanism shown in Fig. 1(d). It is kinematically decoupled.

Based on the idea above, the parallel-kinematic nanopositioning stage is developed with a monolithic compliant mechanical structure and two PZTs, as shown in Fig. 3(a). The compliant mechanical structure has two kinematic chains and each kinematic chain is composed of two flexure modules. The flexure module comprises a fixed-fixed beam and a parallelogram flexure which serve as the prismatic joints P_1 and P_2 shown in Fig. 1(d). The fixed-fixed beams are used to provide large stiffness so as to achieve high resonance frequencies for the developed stage. The parallelogram flexures are distributed symmetrically around the end-effector to decouple the motion between two axes and restrict parasitic motion in the XY plane. When the stage is actuated along the X-axis as shown in Fig. 3(b), the translational motion of the end-effector is provided by the deformation of fixed-fixed beams in X-axis and accommodated by the parallelogram flexures in Y-axis, and vice versa. Due to the symmetric mechanical structure, the stiffness and dynamic performance of the stage along X- and Y-axis are the same.

To achieve high resonance frequencies and decoupled performance simultaneously, large stiffness should be distributed properly between the fixed-fixed beam and the parallelogram flexure. First, large stiffness ratio between the fixed-fixed beam and the parallelogram flexure should be ensured. In the above kinematic analysis, the motion of the end-effector along X-axis is considered to be accommodated by the parallelogram flexures in Y axis, and thus the stage is decoupled. At this point, the fixed-fixed beams in Y-axis are assumed as static rigid bodies as well as the fixed base. However, this assumption is valid only when the fixed-fixed beam has much larger stiffness than the parallelogram flexure in the same flexure module. Otherwise, movement of parallelogram flexures would cause deformation of the fixed-fixed beams in

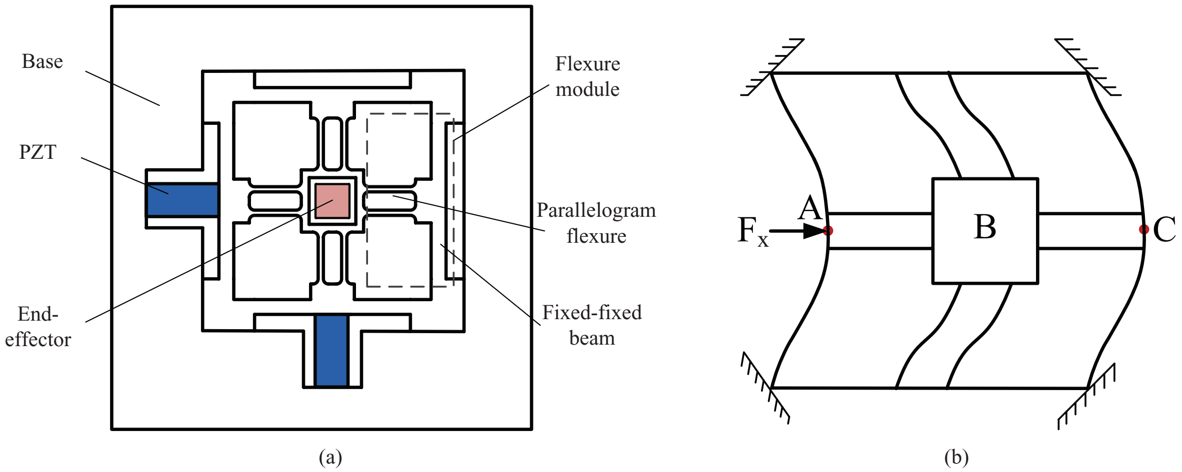

FIG. 3. The XY nanopositioning stage. (a) Mechanical structure of the stage. (b) Simplified schematic representation of the deformed stage when it is actuated along X-axis.

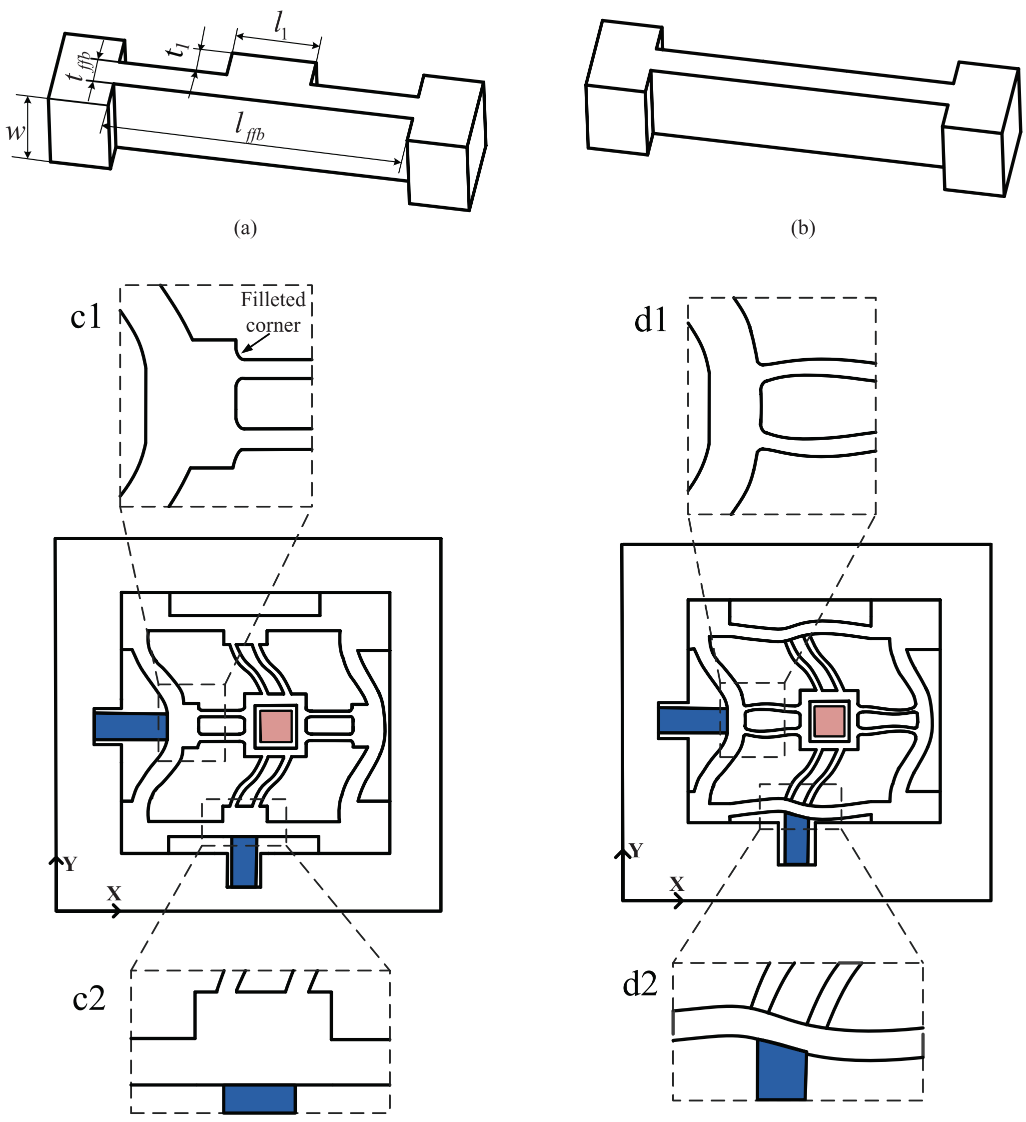

(a) (b)

(c) (d)

FIG. 4. Fixed-fixed beam design. (a) CT beam. (b) CRCS beam. (c) Flexure deformation using CT beam. (d) Flexure deformation using CRCS beam.

Y-axis. This results in cross-coupling when the stage is actuated along Y-axis at the same time. Second, the stiffness of the parallelogram flexures should not be too small. It has to be ensured that local vibration mode with low resonance frequency is not introduced. Therefore, selecting fixed-fixed beams and parallelogram flexures with proper stiffness is crucial.

For the fixed-fixed beam, it is a common practice to utilize the constant rectangular cross section beam[2,11,14] (CRCS beam, as shown in Fig. 4(b)). With the purpose to ensure good performance for the developed stage, a novel center-thickened beam (CT beam, as shown in Fig. 4(a)) is designed in this paper to act as the fixed-fixed beam. Compared with the commonly used constant rectangular cross section beam, the CT beam has several advantages. First, when the stage is actuated in one direction (e.g., in X-axis), a CT beam provides nearly pure translational motion for the parallelogram flexure connected to it, as depicted in rectangular c1 in Fig. 4(c). On the contrary, a CRCS beam would cause undesired bend of the parallelogram flexure besides translational motion, as depicted in rectangular d1 in Fig. 4(d). Such undesirable deformation will result in unexpected cross-coupling when the stage is actuated in the other direction at the same time. Second, a CT beam has larger stiffness than the CRCS beam when the dimensional parameters are the same. Larger stiffness contributes to improving the resonance frequencies of the developed stage and larger stiffness ratio between fixed-fixed beam and parallelogram flexure helps decouple the motion between two axes. Third, a CT beam with large stiffness would protect the PZT from damage caused by bending moment. When the stage is actuated in X-axis, the parallelogram flexures in Y-axis also apply bending moment on the fixed-fixed beams in Y-axis. Thus, insufficient stiffness of the fixed-fixed beams would result in unexpected twisting as shown in rectangular d2 in Fig. 4(d). Such twisting will produce a bending moment on the PZT in Y-axis, which could damage the PZT.[20,21] Such disadvantage would be avoided when the CT beam is utilized, as shown in rectangular c2 in Fig. 4(c), since it can provide sufficient stiffness.

For the parallelogram flexure, three types of flexures could be utilized, i.e., the distributed-compliance flexure, the lumped-compliance flexure, and the hybrid compliant-notch flexure.[22] Considering the achievable stiffness, structural frequency and tolerance to manufacturing error, the distributed-compliance flexure is superior than the others and thus it is widely used in the stage design.[2,14,23] In the development, the distributed-compliance flexure is chosen as the parallelogram flexure. Besides, to reduce the stress concentrations at the flexure ends, the flexures are designed to be corner-filleted,[24] as shown in Figs. 3(a) and 4(c).

B. Static and dynamic analysis

The static model of the developed stage is established without taking the PZTs into account. The stiffness of the stage along X-axis and Y-axis[25] is $K_x = K_y = 2(K_{ffb} + K_{pf})$, where K_{ffb} and K_{pf} are the stiffness of fixed-fixed beam and parallelogram flexure, respectively. K_{ffb} and K_{pf} are derived by using Castigliano's second theorem. This method is commonly used in the flexure analysis literature.[13,14,26] K_{ffb} is expressed as

$$K_{ffb} = 1 \Big/ \left[\frac{l_1^3 - 6cl_1^3}{48EI_1} + \frac{\left(l_{ffb}^3 - l_1^3\right) - 6c\left(l_{ffb}^2 l_1 - l_1^3\right)}{48EI_2} + \frac{\beta l_1}{4GA_1} + \frac{\beta(l_{ffb} - l_1)}{4GA_2} \right], \tag{1}$$

where E is Young's modulus of beam material, G is the shear modulus, β is a coefficient related to the shape of the cross section (for a rectangular cross section $\beta = 1.2$); $I_1 = w(t_{ffb} + t_1)^3/12$, $I_2 = wt_{ffb}^3/12$, $A_1 = w(t_{ffb} + t_1)$, $A_2 = wt_{ffb}$, $c = [l_1^2 I_2 + (l_{ffb}^2 - l_1^2)I_1]/\{8[l_1^2 I_2 + (l_{ffb}l_1 - l_1^2)I_1]\}$. For K_{pf}, it is also obtained using the same method as addressed for K_{ffb}.

Lagrange's equation is used for the dynamics modeling of the stage. The dynamics equation of the undamped free vibration of the XY stage without PZTs is obtained as[25] $\mathbf{M}\ddot{\mathbf{q}} + \mathbf{K}\mathbf{q} = 0$, where $\mathbf{M} = diag(M_x^e, M_y^e)$ (M_x^e and M_y^e are the total equivalent mass of the stage in X- and Y-axis), $\mathbf{K} = diag(K_x, K_y)$, and $\mathbf{q} = [\Delta x, \Delta y]^T$ (Δx and Δy are the displacements of the end-effector in X-axis and Y-axis). Since $\mathbf{K}$ and $\mathbf{M}$ are diagonal matrixes, it is demonstrated that the two axes of the stage are decoupled. Solving the characteristic equation, and then the natural frequencies f_i of the mechanical structure is derived, i.e.,

$$|\mathbf{K} - \mathbf{M}\lambda_i| = 0; \qquad f_i = 1/(2\pi)\sqrt{\lambda_i}. \tag{2}$$

When the PZT is taken into account, the fundamental natural frequency of the whole system in X-axis and Y-axis can be approximately calculated by[25]

$$\bar{f_i} = \frac{1}{2\pi}\sqrt{\frac{K_s + K_p}{M_s + M_p}}, \tag{3}$$

where $M_s (M_s = M_x^e = M_y^e)$, M_p, $K_s (K_s = K_x = K_y)$, and K_p are, respectively, the equivalent mass and stiffness of the stage and PZT.

III. DESIGN CONSIDERATIONS, DIMENSIONAL OPTIMIZATION, AND FINITE ELEMENT ANALYSIS

A. Design considerations

The stage is designed to achieve high resonance frequencies (no less than 8 kHz without PZTs), relatively large workspace (over 10 μm × 10 μm) and decoupled performance between X- and Y-axis. Besides, the first two vibration modes should occur in the two actuation directions and they are expected to be as high as possible since they are directly related to the dynamic performance of the stage.

To achieve the dsired travel range, two Noliac NAC 2021-H12 piezoelectric stack actuators (7 mm × 7 mm × 12 mm, 1050 nF) are chosen. The free stroke, stiffness, and blocking force of the actuator are 14.7 μm, 140 N/μm, and 2060 N, respectively. As the piezoelectric stack actuators are made of multiple piezoelectric layers glued together, they are sensitive to pulling forces which may damage them. Hence, preload must be applied to the actuators to protect them from the pulling forces. In the developed stage, the actuators are assembled between the fixed-fixed beam and a preload baffle (as shown in Fig. 8(a)). Preload is provided by the restoring force of the deformed flexures.

To ensure high resonance frequencies of the stage, body material with high ratio of Young's Modulus (E) to density (ρ) is preferred. In this work, aluminum 7075 is chosen. Its Young's modules, density, and yield stress are 71.7 GPa, 2810 kg/m^3, and 500 MPa, respectively.

B. Dimensional optimization

According to the analysis in Sec. II, the dimensions of the stage are critical to the static and dynamic performance. Therefore, it is necessary to optimize the dimensions so as to obtain an ideal structure. The objective of the optimization is to maximize the first resonance frequency f of the mechanical structure and the variables to be optimized are the dimensional parameters of l_{ffb}, t_{ffb}, l_{spf}, and t_{spf}. l_{ffb} and t_{ffb} are the parameters of the CT beam, as illustrated in Fig. 4(a). l_{spf} and t_{spf} are the length and thickness of each beam in parallelogram flexure. The constraints of the optimization are described as follows.

(1) Workspace of the stage: The designed maximum workspace of the stage $\Delta L \times \Delta L$ should be larger than the objective value. The maximum displacement of the stage is

$$\Delta L = \frac{K_p \Delta L_{nom} - F_{pre}}{K_s + K_p} > 10.5\,\mu\text{m}, \tag{4}$$

where ΔL_{nom} is the maximum nominal displacement of the PZT, F_{pre} is the preload applied on the PZT chosen as 200 N (recommended by the manufacturer), K_p and K_s are the translational stiffness of PZT and the stage, respectively. In order to guarantee the travel range of the stage (10 μm × 10 μm), the designed displacement threshold is conservatively chosen as 10.5 μm.

(2) Maximum stress: The maximum stress generated inside the compliant mechanical structure should always be

kept within the maximum allowable stress of the material, i.e.,

$$\sigma_{\max}^{ffb} = \alpha \frac{12\Delta d_{\max}^{ffb} E t_{ffb}}{l_{ffb}^2} \le [\sigma] = \frac{\sigma_y}{n}, \qquad (5)$$

$$\sigma_{\max}^{spf} = \alpha \frac{3\Delta d_{\max}^{spf} E t_{spf}}{l_{spf}^2} \le [\sigma], \qquad (6)$$

where α is the stress concentration factor chosen as 2, $\Delta d_{\max}^{ffb}$ and $\Delta d_{\max}^{spf}$ are the maximum displacement of the fixed-fixed beam and parallelogram flexure ($\Delta d_{\max}^{ffb} = \Delta d_{\max}^{spf} = \Delta L$), σ_y is the yield stress of the material, and n is the safety factor chosen as 2.

(3) Stiffness ratio between the fixed-fixed beam and parallelogram flexure: The stiffness of the fixed-fixed beam should be much larger than that of the parallelogram flexure to ensure the decoupled performance. Meanwhile, the stiffness of the parallelogram flexure should not be too small, and thus the stiffness ratio is chosen as

$$20K_{pf} > K_{ffb} > 10K_{pf}. \qquad (7)$$

(4) Ranges of parameters: The thickness of the stage (w) is chosen as 10 mm to guarantee the stiffness of the developed stage in Z-axis. To protect the beams in parallelogram flexures from stress concentration, the corner radius at the beam ends is chosen as 1 mm. In order to determine the size ($l_1 \times t_1$) of rectangular lump in the fixed-fixed beam, finite element analysis is performed over a wide range of parameters. Finally $l_1 \times t_1$ is chosen as 8.42 mm × 3 mm to guarantee the benefits of the CT beam shown in Sec. II and restrict the equivalent mass simultaneously. The ranges of other dimensions are chosen as follows: $30\ \text{mm} \le l_{ffb} \le 45\ \text{mm}$, $1.5\ \text{mm} \le t_{ffb} \le 5\ \text{mm}$, $10\ \text{mm} \le l_{spf} \le 15\ \text{mm}$, $0.8\ \text{mm} \le t_{spf} \le 1.5\ \text{mm}$. The lower bounds of the dimensions are set to ensure the performance requirements of the developed stage, and the upper bounds are set to achieve a compact structure.

The optimization is carried out with the "fmincon" function in MATLAB, and the optimal results are: $l_{ffb} = 30$ mm, $t_{ffb} = 2.76$ mm, $l_{spf} = 10$ mm, and $t_{spf} = 1$ mm. Based on the optimized dimensions, the analytical results of static and dynamic performance of the stage can be obtained by (2)–(4). The results show that the stage has a workspace of 10.7 μm × 10.7 μm and stiffness of 33.5 N/μm along both X- and Y-axis. Besides, the first resonance frequency of the stage without and with PZTs are 8844 Hz and 15 691 Hz, respectively.

C. Finite element analysis

FEA is generally used to analyze the static and dynamic performance of flexure-guided stages during the design process.[4,10,14,16] In this work, FEA is carried out using ANSYS WorkBench software. The stiffness, workspace, decoupled performance, stress distribution, and dynamic behavior of the stage are studied, respectively.

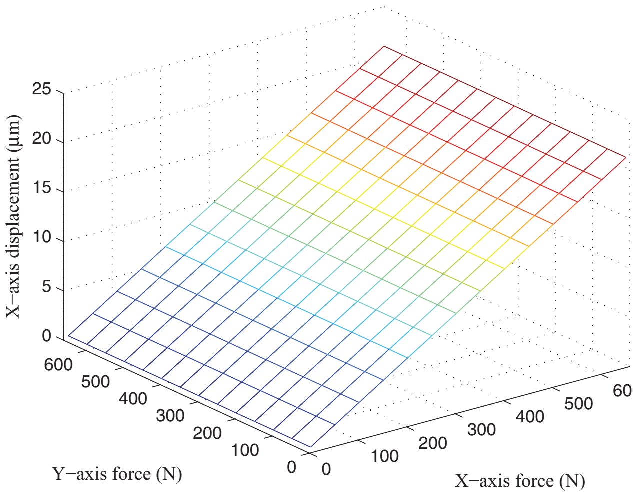

FIG. 5. FEA results of force-displacement relationship.

Fig. 5 shows the FEA results of the force-displacement relationship. From the figure, it can be seen that the displacement of the end-effector along X-axis increases linearly with the increase of the X-axis actuating force. The stiffness along X-axis is 31.4 N/μm. Considering (4), the maximum displacement of the stage along X-axis is 10.8 μm. The stiffness and maximum displacement of Y-axis are obtained by the same way addressed for X-axis and are equal to those of X-axis.

In Fig. 5, the displacement of X-axis is constant (nearly zero) when the actuation force of Y-axis increases. It indicates that the stage has decoupled performance, which agrees with the dynamic analysis in Sec. II.

To test the stress distribution, an input force $F = [600\,\text{N}, 600\,\text{N}]$ is applied to the stage. The von-mises stress distribution is shown in Fig. 6. It can be seen that the maximum von-mises stress is 66.3 MPa occurring near the rectangular lump in the PZT-actuated fixed-fixed beam. It is much lower than the allowable stress (250 MPa) of the body material, which indicates that the stage can achieve a larger workspace without material failure.

The modal analysis is carried out and the results are shown in Fig. 7. As can be seen, the first two modes are the translational modes and the resonance frequencies are over 8.2 kHz, which satisfies the design requirement. Besides, the resonance frequencies of the first two modes are almost the same because of the symmetric structure of the stage.

Table I shows the comparison of analytical and FEA results. As can been seen, the analytical stiffness and resonance frequencies are larger than the FEA value. The main reason for the overestimation lies in that, in the static and dynamic analysis, the fixed-fixed beams in one axis are assumed to be rigid bodies when the stage is actuated in the other axis. However, in practice, they are not strictly rigid bodies due to the limited stiffness. Such overestimation problem can also be found in other reported works.[4,10,16] Nevertheless, in this work, the analytical results are within

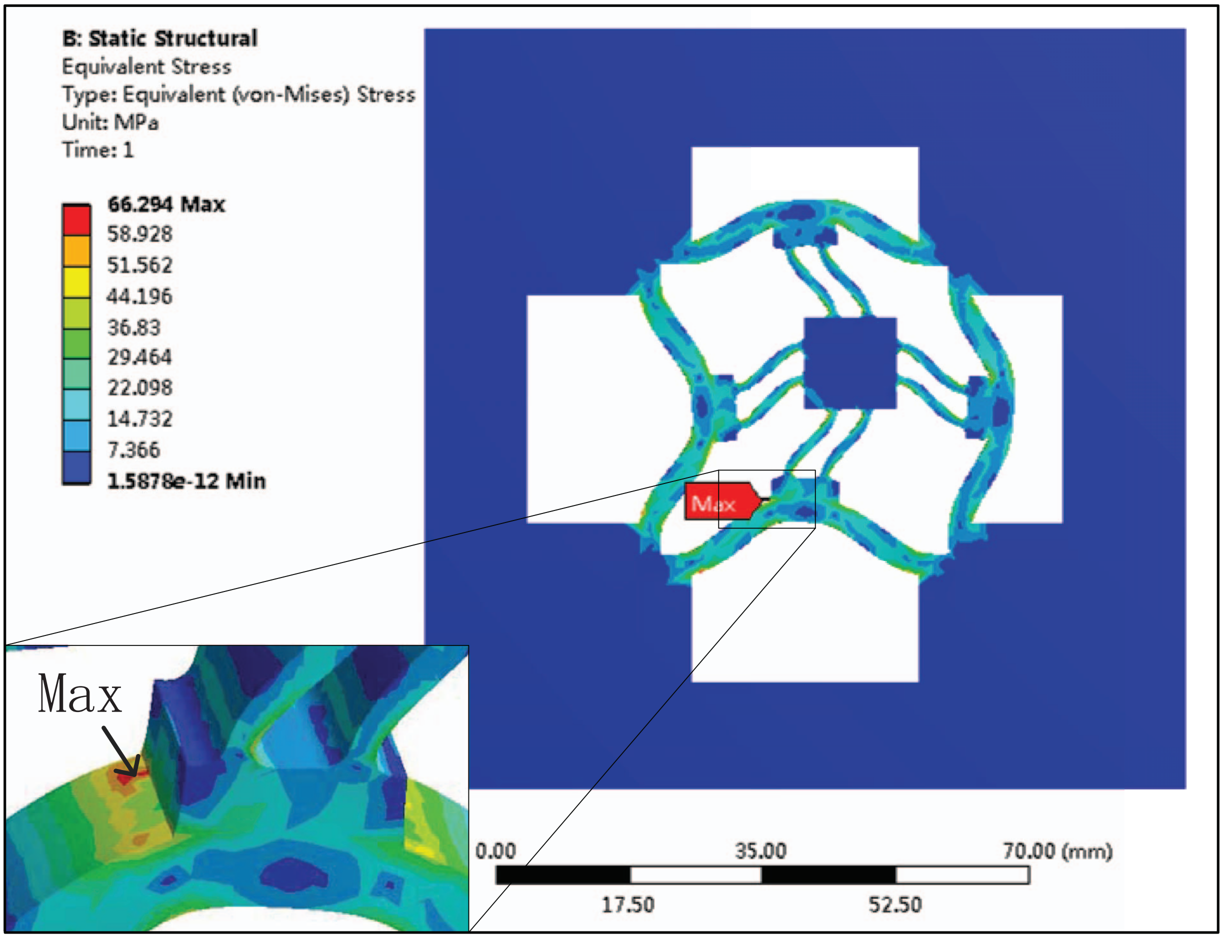

FIG. 6. Von-mises stress distribution under maximum actuating force.

reasonable agreement with the FEA results. It should be mentioned that only the stage without PZTs assembled are analyzed by ANSYS, as it is quite difficult to model the PZTs accurately. The resonance frequencies of the stage including PZTs will be directly tested by experiments in Sec. IV B.

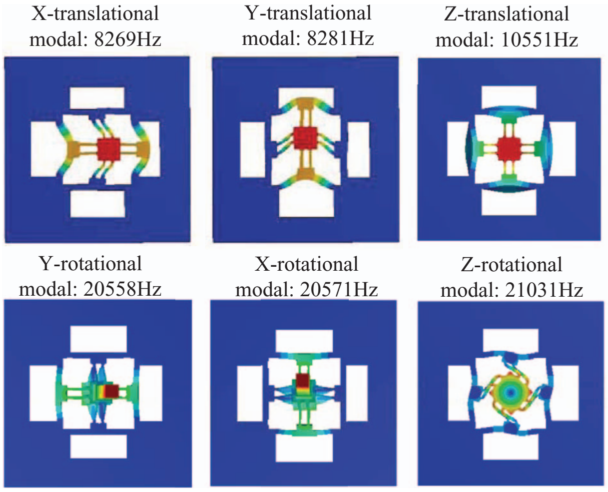

FIG. 7. Modal analysis results by FEA.

IV. EXPERIMENTAL SETUP AND PERFORMANCE TESTS

A. Experimental setup

Fig. 8(a) shows the experimental setup. A prototype of the XY stage is fabricated using wire electrical discharge machining (WEDM) technique with aluminum 7075. The two pre-selected PZTs are mounted to drive the stage, and a dual-channel high-voltage amplifier (HVA) with a fixed gain of 20 is used to provide excitation voltage (0–200 V) for the PZTs. Two capacitive sensors (Probe 2823 and Gauging Module 8810 from MicroSense, range of +/−10 μm with analog output of +/−10 V) are adopted to measure the displacements of the end-effector along X- and Y-axis. A dSPACE-DS1103 board equipped with the 16-bit analog to digital converters (ADCs) and 16-bit digital to analog converters (ADCs) is

TABLE I. Comparison of analytical results and FEA results.

	K_x (N/μm)	K_y (N/μm)	ΔL_x (μm)	ΔL_y (μm)	f_1 (Hz)	f_2 (Hz)
Analytical results	33.5	33.5	10.7	10.7	8844	8844
FEA results	31.4	31.4	10.8	10.8	8269	8281
Error (%)	6.69	6.69	0.93	0.93	6.95	6.80

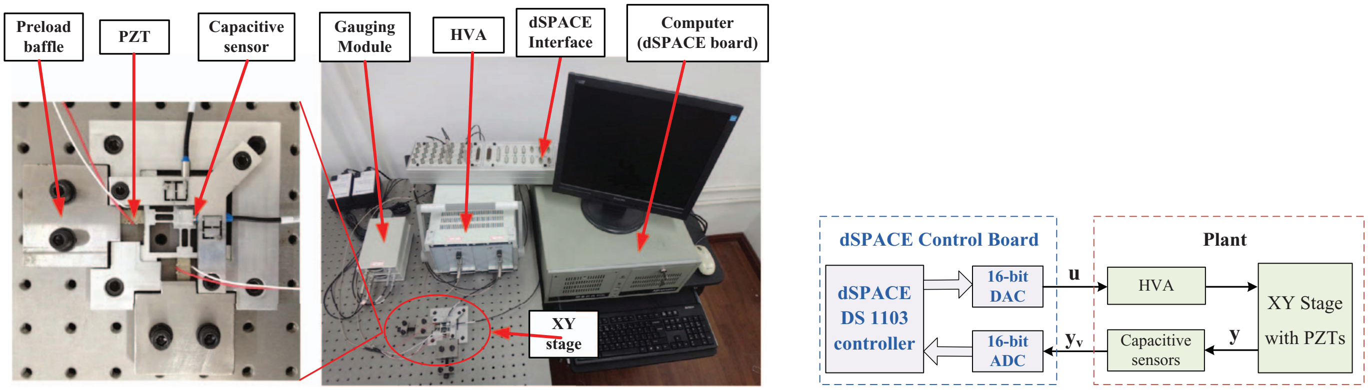

(a) (b)

FIG. 8. The experimental setup. (a) Experimental platform. (b) Block diagram.

utilized to output the excitation voltage for the HVA and capture the real-time displacement information from the capacitive sensors. The block diagram of the whole experimental setup is shown in Fig. 8(b).

B. Static and dynamic performance tests

First, the static performance of the developed stage is evaluated. Fig. 9(a) shows the maximum displacements test results. It can be seen that the maximum displacements of X- and Y-axis are 11.2 μm and 11.6 μm, respectively, which satisfy the design requirements. The experimental results are a little larger than the FEA results, which is due to the preload applied to the PZTs. The preload is considered to be 200 N in the analytical modeling and FEA, but it may be less in practice as it is difficult to measure. From Fig. 9(a), the hysteresis effect of the nanopositioning stage can be observed, which is caused by the inherent nonlinear characteristics of the PZTs.[27] The test of cross-coupling between two axes is also performed and the results are shown in Fig. 9(b). It can be seen that the maximum cross-couplings in Y- and X-axis are 0.058 μm and 0.035 μm, accounting for 0.52% and 0.3% of the maximum displacements, respectively. The small cross-couplings indicate that the developed stage achieves nearly decoupled performance.

To obtain the dynamic characteristic of the stage, a band-limited white noise signal with amplitude of 100 mV and frequency range of 10 Hz to 25 kHz is utilized to excite the stage. The low amplitude is intended to minimize the effect of hysteresis. The inputs are denoted as V_x and V_y (in volts), and the outputs are D_x and D_y (in micrometers). With the system identification toolbox of MATLAB, the frequency responses of $G_{xx} = D_x(s)/V_x(s)$, $G_{yx} = D_y(s)/V_x(s)$, $G_{xy} = D_x(s)/V_y(s)$, and $G_{yy} = D_y(s)/V_y(s)$ are shown in Fig. 10. The dynamic models of G_{xx} and G_{yy} are identified as

$$G_{xx} = \frac{1.742 \times 10^4 s^4 - 2.015 \times 10^9 s^3 + 2.468 \times 10^{14} s^2 - 1.32 \times 10^{19} s + 3.736 \times 10^{23}}{s^5 + 6.822 \times 10^4 s^4 + 1.202 \times 10^{10} s^3 + 5.682 \times 10^{14} s^2 + 3.218 \times 10^{19} s + 5.841 \times 10^{23}}, \tag{8}$$

$$G_{yy} = \frac{1.78 \times 10^4 s^4 - 2.012 \times 10^9 s^3 + 2.491 \times 10^{14} s^2 - 1.322 \times 10^{19} s + 3.734 \times 10^{23}}{s^5 + 6.542 \times 10^4 s^4 + 1.232 \times 10^{10} s^3 + 5.648 \times 10^{14} s^2 + 3.212 \times 10^{19} s + 5.469 \times 10^{23}}. \tag{9}$$

The model simulation results are also shown in Figs. 10(a) and 10(d) to demonstrate the effectiveness of identified models. From the figures, it can be seen that the identified models capture the dynamics of the system accurately in the frequency range of 100 Hz to 16 kHz. It can also be observed that the first resonant peaks of the stage along X- and Y-axis occur at 13.6 kHz and 14.4 kHz, respectively. They are lower than the predicted value (15.7 kHz) in dynamic analysis. This may be caused by PZTs assembling error and machining imperfections. From Figs. 10(b) and 10(c), it can be seen that the magnitude of the dynamic cross-coupling terms G_{yx} and G_{xy} are about -44 dB and -55 dB less than those of G_{xx} and G_{yy}, respectively, confirming the decoupled performance of the stage.

C. Tracking performance tests

The tracking performance of the developed stage is tested. First, tracking of triangular trajectory is carried out with the simplest feedforward method, i.e., DC-gain inversion.[12,28] The peak-to-peak amplitude of the triangular waveform is 0.6 μm and the fundamental frequencies are 100 Hz, 1000 Hz, and 2000 Hz. The tracking trajectories are

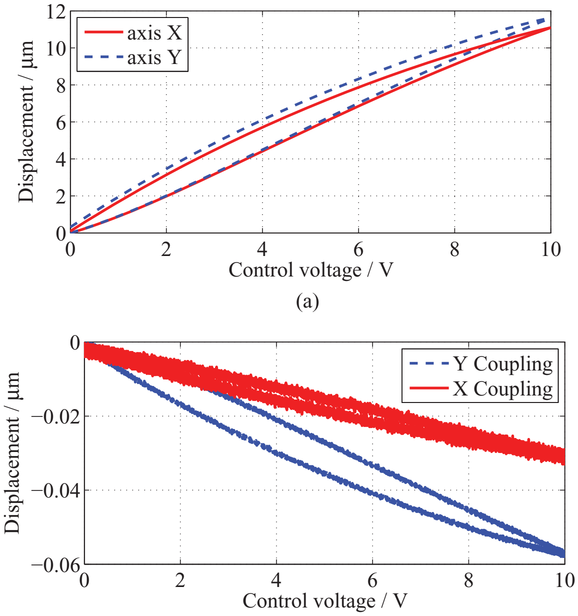

(a)

(b)

FIG. 9. Experimental results of maximum displacements and cross-coupling displacements. (a) Maximum displacements of the stage. (b) Cross-coupling displacements of the stage.

constructed using the first seven odd harmonics (first, third, fifth, seventh, ninth, eleventh, and thirteenth). The experimental results are shown in Figs. 11(a), 11(c), and 11(e). It is observed that the stage achieves accurately tracking at 100 Hz. However, the tracking performance becomes worse with the increase of trajectory fundamental frequencies and the vibration is obvious at frequency of 2000 Hz, which can be seen from Fig. 11(e).

To eliminate the vibration in high-speed tracking, an inversion-based feedforward approach is employed. It is a well-known control approach for vibration compensation and widely used in the literature.[28,29] For a desired trajectory, the feedforward input is derived by inverting the dynamics of the stage. For a periodic triangular trajectory $p_d(t) = B + \sum_{k=1}^{\infty} A_k \sin(\omega_k t)$ (B is the bias, $A_k = 8A \cdot (-1)^{(k-1)/2}/(k^2\pi^2)$, and A is the amplitude), the feedforward input is $u_{ff}(t) = \frac{B}{G_{xx}(0)} + \sum_{k=1}^{\infty} \frac{A_k}{|G_{xx}(i\omega_k)|} \sin(\omega_k t - \phi_k)$ ($\phi_k = \angle G_{xx}(i\omega_k)$). Figs. 11(b), 11(d), and 11(f) show the experimental results. From the figure it can be observed that no vibration occurs at 2000 Hz which demonstrates that the inversion-based feedforward approach well compensates for the vibration. In Table II, the tracking performance of the DC-gain inversion and model-based inversion feedforward

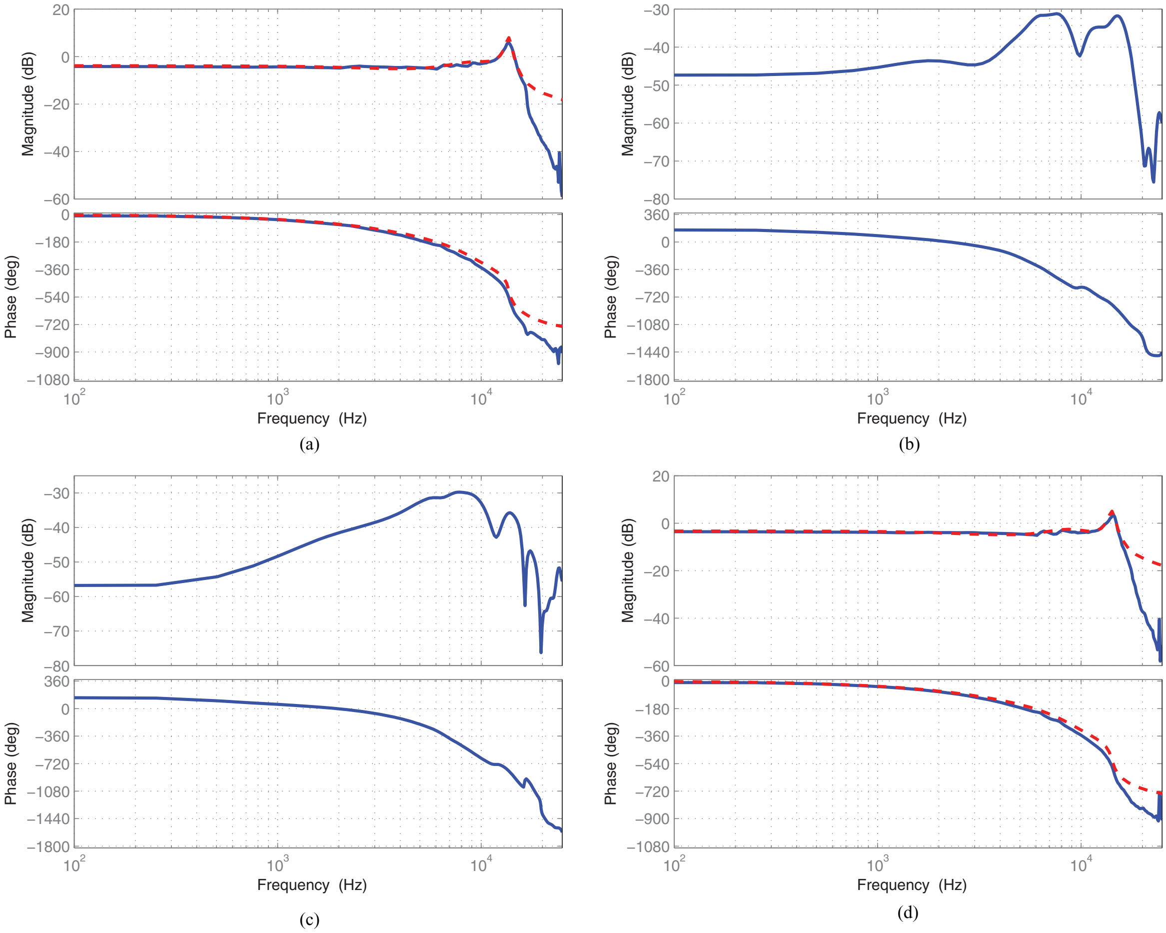

(a)

(b)

(c)

(d)

FIG. 10. Frequency responses of the XY stage. The dashed lines in (a) and (d) are model simulation results, and the solid lines are experimental results. (a) G_{xx}; (b) G_{yx}; (c) G_{xy}; and (d) G_{yy}.

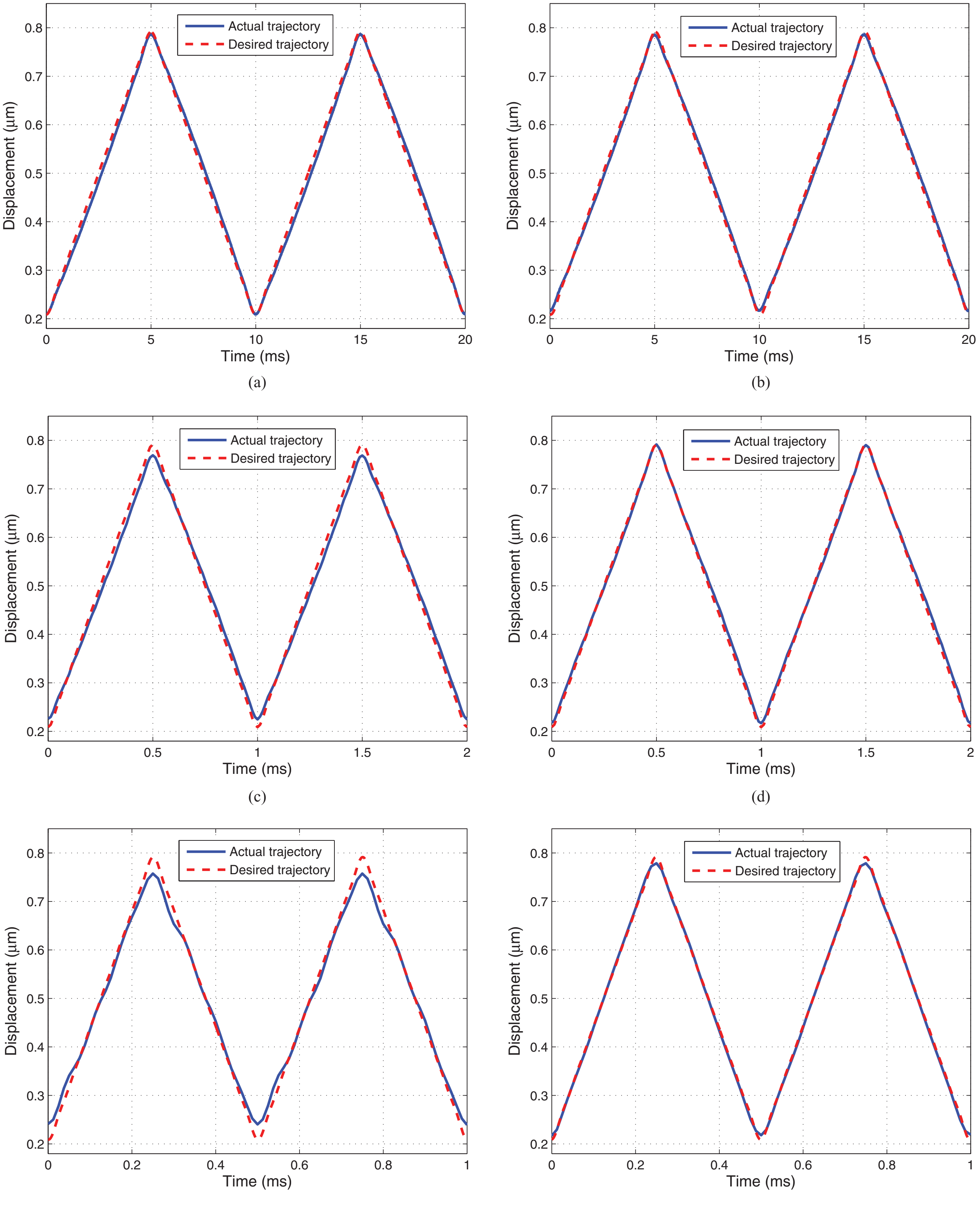

(a) (b)

(c) (d)

(e) (f)

FIG. 11. Tracking performance for triangular trajectories under various input frequencies. (a), (c), and (e) show the tracking results with the DC-gain inversion at 100 Hz, 1000 Hz, and 2000 Hz. (b), (d), and (f) show the tracking results with the inversion-based feedforward approach at 100 Hz, 1000 Hz, and 2000 Hz.

TABLE II. Tracking performance at various frequencies.

Frequency (Hz)	DC-gain approach (MTE/RMSTE, %)	Inversion-based approach (MTE/RMSTE, %)
100	3.18/1.25	2.22/1.25
1000	3.75/2.4	2.35/1.17
2000	5.65/2.87	2.1/0.93

approach is summarized in terms of the maximum tracking error (MTE) and root-mean-square tracking error (RMSTE).[30] It can be observed that the tracking performance is improved with the inversion-based feedforward approach compared to the DC-gain inversion.

It should be noted that in the tracking performance tests the sampling frequency of the dSPACE is set to 80 kHz, which is nearly its maximum sampling frequency. The limitation in sampling frequency makes it difficult for the developed stage to carry out tracking tests at a higher speed. Such limitation is also encountered in other works.[14] Development of hardware with high sampling frequency will be the future work.

D. Comparison with the other stages

Table III illustrates the comparison between the developed stage and other high-bandwidth parallel-kinematic nanopositioning stages[2,11,14] in terms of the fixed-fixed beam type, PZTs number in X- and Y-axis, workspace, the first resonance frequency, and X/Y cross-coupling. It is observed that, with the proposed CT beam, the stage developed in this work offers the lowest static and dynamic cross-coupling and possesses the highest first resonance frequency among the stages using the same number of PZTs in X- and Y-axis. This shows the advantage of the developed stage and the proposed CT beam. It should be noted that the stage in Ref. 2 uses four PZTs in X-/Y-axis (much more than the other stages) and thus has a higher resonance frequency. However, this would require costly high-power voltage amplifiers to drive these PZTs. It can be seen from Table III that the workspace of stage developed in this work is a little smaller than that of the stages in Refs. 2 and 11. This is due to the design objective (10 μm × 10 μm) and the selected displacement threshold in Eq. (4) in Sec. III. To improve the workspace, a larger displacement threshold can be chosen, while this might cause decrease in the resonance frequency of the stage. In addition, PZTs with larger free stroke and stiffness can be adopted to drive the stage to achieve a larger workspace.

TABLE III. Comparison of typical high-bandwidth parallel-kinematic nanopositioning stages.

Reference	Schitter[2]	Polit[11]	Yong[14]	This work
Fixed-fixed beam type	CRCS	CRCS	CRCS	CT
PZTs number in X-/Y-axis	4/4	1/1	1/1	1/1
Workspace (μm × μm)	13 × 13	15 × 15	6.5 × 6.6	11.2 × 11.6
The first resonance frequency (kHz)	22	8	8.8	13.6
X/Y static cross-coupling (%)	N/A	N/A	3.1/2.5	0.3 /0.52
X/Y dynamic cross-coupling (dB)	N/A	−40/−40	−29.9/−31.8	−55/−44

V. CONCLUSIONS

In this paper, a piezo-driven high-bandwidth XY nanopositioning stage with parallel-kinematic mechanism is developed. The design, analysis, and experimental verification are presented. The stage is designed with two kinematic chains and each kinematic chain is composed of two symmetrically distributed special flexure modules. In each flexure module, a fixed-fixed beam and a parallelogram flexure serve as two orthogonal prismatic joints. To achieve high resonance frequencies, a novel center-thickened beam, which has larger stiffness than the commonly used constant rectangular cross-section beam, is proposed to act as the fixed-fixed beam. The center-thickened beam also helps reduce the cross-coupling between two axes. To decouple the motion in two axes totally, a symmetric configuration is adopted for the parallelogram flexures. The static and dynamic models of the developed stage are established. Based on the models, dimensional optimization is performed to maximize the first resonance frequency. FEA is then used to validate the design and a prototype is fabricated for experimental validation. The results of static and dynamic tests show that the resonance frequencies of the developed stage are over 13.6 kHz and the workspace is 11.2 μm × 11.6 μm with the maximum cross-coupling between X- and Y-axis lower than 0.52%. According to the results of high-speed tracking tests with an inversion-based feedforward controller, high-precision triangular trajectory tracking up to 2000 Hz is achieved by the stage. In summary, the developed stage achieves excellent performances such as high resonance frequencies, relatively large travel range, decoupled motion in two axes, and high-precision and high-speed trajectory tracking. Future works will focus on: (1) design of advanced control strategy including closed-loop control and hysteresis compensation for high-speed and high-amplitude trajectory tracking; (2) development of hardware with high sampling frequency.

ACKNOWLEDGMENTS

This work was supported by the National Natural Science Foundation of China (Grant No. 91023047) and the "Shu Guang" project supported by Shanghai Municipal Education Commission (Grant No. 10SG17) and Specialized Research Fund for the Doctoral Program of Higher Education (Grant No. 20130073110037).

[1] D.-M. Kim, D.-W. Kang, J.-Y. Shim, I.-C. Song, and D.-G. Gweon, Rev. Sci. Instrum. **76**, 073706 (2005).
[2] G. Schitter, K. J. Astrom, B. E. DeMartini, P. J. Thurner, K. L. Turner, and P. K. Hansma, IEEE Trans. Control Syst. Technol. **15**, 906 (2007).
[3] K. K. Leang and A. J. Fleming, Asian J. Control **11**, 144 (2009).
[4] K.-B. Choi and J. J. Lee, Rev. Sci. Instrum. **76**, 075106 (2005).
[5] Y. K. Yong and T.-F. Lu, Mech. Mach. Theory **44**, 1156 (2009).
[6] S. Verma, W.-J. Kim, and H. Shakir, IEEE Trans. Ind. Appl. **41**, 1159 (2005).
[7] T. Ando, N. Kodera, D. Maruyama, E. Takai, K. Saito, and A. Toda, Jpn. J. Appl. Phys. **41**, 4851 (2002).

[8] H.-Y. Kim, D.-H. Ahn, and D.-G. Gweon, Rev. Sci. Instrum. **83**, 055114 (2012).

[9] Y. K. Yong, T.-F. Lu, and D. C. Handley, Precis. Eng. **32**, 63 (2008).

[10] L.-J. Lai, G.-Y. Gu, and L.-M. Zhu, Rev. Sci. Instrum. **83**, 045105 (2012).

[11] S. Polit and J.-Y. Dong, IEEE/ASME Trans. Mechatron. **16**, 724 (2011).

[12] Y. K. Yong, S. O. R. Moheimani, B. J. Kenton, and K. K. Leang, Rev. Sci. Instrum. **83**, 121101 (2012).

[13] B. J. Kenton and K. K. Leang, IEEE/ASME Trans. Mechatron. **17**, 356 (2012).

[14] Y. K. Yong, B. Bhikkaji, and S. O. R. Moheimani, IEEE/ASME Trans. Mechatron. **18**, 1060 (2013).

[15] H. Watanabe, T. Uchihashi, T. Kobashi, and M. Shibata, Rev. Sci. Instrum. **84**, 053702 (2013).

[16] Y.-M. Li and Q.-S. Xu, IEEE Trans. Robot. **25**, 645 (2009).

[17] S. Awtar, A. H. Slocum, and E. Sevincer, ASME J. Mech. Des. **129**, 625 (2007).

[18] Q. Yao, J. Dong, and P. M. Ferreira, Int. J. Mach. Tools Manuf. **47**, 946 (2007).

[19] Y.-M. Li and Q.-S. Xu, IEEE Trans. Autom. Sci. Eng. **3**, 247 (2006).

[20] See http://www.noliac.com/Default.aspx for Noliac actuators datasheet.

[21] Y.-M. Li, J.-M. Huang, and H. Tang, IEEE Trans. Autom. Sci. Eng. **9**, 538 (2012).

[22] S. Polit and J.-Y. Dong, J. Manuf. Syst. **28**, 71 (2009).

[23] Y. K. Yong, S. S. Aphale, and S. O. R. Moheimani, IEEE Trans. Nanotechnol. **8**, 46 (2009).

[24] N. Lobontiu, J. S. N. Paine, E. Garcia, and M. Goldfarb, ASME J. Mech. Des. **123**, 346 (2001).

[25] C.-X. Li, G.-Y. Gu, M.-J. Yang, and L.-M. Zhu, in *Intelligent Robotics and Applications*, Lecture Notes in Computer Science Vol. 8103 (Springer, Berlin/Heidelberg, 2013), pp. 678–689.

[26] Y. K. Yong and T.-F. Lu, Mech. Mach. Theory **43**, 347 (2008).

[27] G.-Y. Gu, L.-M. Zhu, C.-Y. Su, and H. Ding, IEEE/ASME Trans. Mechatron. **18**, 1459 (2013).

[28] G. M. Clayton, S. Tien, K. K. Leang, Q. Z. Zou, and S. Devasia, Trans. ASME, J. Dyn. Syst. Meas. Control **131**, 061101 (2009).

[29] S. S. Aphale, S. Devasia, and S. O. Moheimani, Nanotechnology **19**, 125503 (2008).

[30] G.-Y. Gu and L.-M. Zhu, Rev. Sci. Instrum. **81**, 085104 (2010).